"Ground truth" occurrence of Pink Spinel Anorthosite (PSA) as clasts in lunar meteorite Northwest Africa (NWA) 15500: Chemical evidence for a genetic relationship with lunar highlands Mg-suite and formation by magma–wallrock interactions

Daniel SHEIKH [iD]*, Alex M. RUZICKA [iD], and Melinda L. HUTSON [iD]

Cascadia Meteorite Laboratory, Department of Geology, Portland State University, Portland, Oregon, USA

*Correspondence
Daniel Sheikh, Cascadia Meteorite Laboratory, Department of Geology, Portland State University, 1721 SW Broadway, Portland, OR 97207, USA.
Email: dsheikh@pdx.edu

Abstract–Pink spinel anorthosite (PSA), a distinctive plagioclase and spinel-rich lithology (spinel >20%) observed on the lunar surface by the Moon Mineralogy Mapper (M^3) imaging spectrometer, has sparked considerable interest in understanding magmatic processes on the Moon that cannot be explained by the well-established lunar magma ocean paradigm. Competing ideas on the PSA-forming mechanisms have invoked either (1) impact melting of troctolitic source rocks on the lunar surface or (2) magma–wallrock interactions between anorthositic crust and Mg-suite parental melts, but have been difficult to evaluate given the lack of ground truth samples. Here, we investigate the textures and mineral compositions of seven PSA clasts in lunar meteorite Northwest Africa (NWA) 15500, and the bulk trace element compositions of a PSA clast separate and NWA 15500 host lithologies A and B. Our findings suggest derivation of PSA from an incompatible-element-poor source and are consistent with PSA representing an Mg-suite lithology genetically related to pink spinel troctolites that reflects increased degrees of crustal assimilation during magma–wallrock interactions, and a sourcing of PSA far from the Procellarum KREEP Terrane. Excavation of PSA material was followed by multiple, subsequent localized impact events, resulting in the formation of Lithologies A and B.

INTRODUCTION

Magnesium-rich spinel (near endmember $MgAl_2O_4$, herein referred to as "pink spinel") is generally observed to be an accessory mineral phase in igneous rocks from the Moon, as on Earth. Although several pink spinel-bearing assemblages have been identified in the existing lunar sample collection (e.g., pink spinel troctolites [PST] and spinel cataclasites; Herzberg & Baker, 1980; Papike et al., 1998; Shearer et al., 2015), most contain relatively minor amounts of pink spinel (~5–6 vol%) and all contain significant quantities of mafic minerals (olivine, pyroxene) (Gross, Isaacson, et al., 2014). Exceptions to low spinel

content are a PST clast in Apollo sample 67435 (~13 vol% spinel) (Ma et al., 1981) and a spinel-rich (~30 vol%) clast in lunar meteorite Allan Hills (ALHA) 81005 (Gross & Treiman, 2011).

Therefore, the initial discovery of a unique Mg-spinel lithology along the inner ring of Moscoviense Basin by remote sensing from the M^3 imaging spectrometer aboard Chandrayaan-1 (Pieters et al., 2011) came as an important surprise to our current understanding of spinel formation on the Moon. This Mg-spinel lithology, coined "pink spinel anorthosite" (PSA) (Pieters et al., 2011), exhibits a reflectance spectra dominated by spinel (~20–30 vol%) and plagioclase feldspar, with minor abundances of mafic

minerals (<5 vol% olivine + pyroxene) (Gross, Isaacson, et al., 2014). As observed by remote sensing, the global distribution of confirmed PSA exposures (each approximately a few hundred meters) along the walls/peaks of impact craters and along inner rings of larger basins on both the nearside and farside of the Moon (Pieters et al., 2014; Prissel et al., 2014) indicate that PSA represents a minor, but relatively important rock type present in the lunar highlands.

This has sparked considerable interest in understanding widespread secondary processes on the Moon that cannot be explained by the well-established lunar magma ocean (LMO) paradigm (Elardo et al., 2011; Elkins-Tanton et al., 2011; Schmidt & Kraettli, 2022; Shearer & Papike, 1999; Warren & Taylor, 2014). Several studies have attempted to recreate PSA through high-temperature crystallization experiments (Gross, Isaacson, et al., 2014; Prissel et al., 2014), yielding two candidate PSA-forming mechanisms: (1) basin-forming impacts into lunar highland troctolitic source rocks that crystallize PSA (Treiman et al., 2019), and (2) magma–wallrock interactions involving assimilation of anorthositic crust (e.g., Ferroan Anorthosites or FANs) into plagioclase-undersaturated picritic or Lunar Highlands High Magnesian Suite (Mg-suite) parental melts at shallow to moderate crustal depths (Gross & Treiman, 2011; Prissel et al., 2014, 2016).

Owing to analytical uncertainty in remote sensing measurements to accurately measure both spinel modal abundance and composition in PSA (Gross et al., 2015; Gross, Isaacson, et al., 2014; Jackson et al., 2014; Williams et al., 2016), evaluating the validity of these formation mechanisms for PSA requires in situ chemical analysis of this lithology. However, "bonafide" PSA material that fits the criteria imposed by remote sensing observations (Pieters et al., 2011) has not been identified in the current lunar sample collection (Elardo et al., 2023), until now. Here, we provide an initial geochemical analysis of seven PSA clasts found within recently classified lunar meteorite Northwest Africa (NWA) 15500. This study represents the first "ground truth" geochemical investigation into the petrogenesis of PSA, and on a larger scale, ultimately provides important implications on the role that interactions between early formed mantle-derived partial melts and anorthositic crust had during the evolution of the lunar interior (Chen et al., 2023; Prissel & Gross, 2020).

Preliminary findings covering some aspects of this work are available in Sheikh et al. (2023).

SAMPLES AND METHODS

Three 27 × 46 mm rectangular polished thin sections (30 μm thick) of NWA 15500 (Cascadia Meteorite Laboratory designations CML 1625-2, 1625-3, and 1625-4) polished with ~1 μm abrasive were prepared by

Spectrum Petrographics. These three thin sections were utilized for the various electron microscopy techniques implemented in this study. A 15–20 nm thick coating of evaporated carbon was applied to the thin sections for scanning electron microscopy (SEM) analysis, which for 1625-3 and 1625-4 was subsequently removed and replaced with a thicker ~30 nm carbon coat for electron microprobe analysis (EMPA). Representative fragments of NWA 15500 Lithologies A and B, each ~175 mg, and an ~100 mg PSA clast separate, were used for obtaining bulk chemical analysis using inductively coupled plasma mass spectrometry (ICP-MS). Images of the samples and thin sections are provided in Figures S1 and S2.

Scanning Electron Microscopy

Electron microscopy of the NWA 15500 thin sections was conducted in the Center for Electron Microscopy and Nanofabrication (CEMN) at Portland State University using a Zeiss Sigma Variable Pressure-Field Emission Gun-Scanning Electron Microscope (VP-FEG-SEM) equipped for energy-dispersive spectroscopy (EDS) with an Oxford Instruments Ultim Max Silicon Drift Detector (SDD).

For EDS analysis, the SEM was operated under high vacuum settings (in high current mode) at a working distance of 8.5 mm using an accelerating voltage of 15 keV, an aperture size of 120 μm, a beam current of ~6–7 nA, and a beam diameter of ~1 μm; all data acquisition was obtained and processed using Oxford Instruments AZtec 6.0 software. Backscattered electron (BSE) images of NWA 15500 Lithology A, Lithology B, and PSA clasts were obtained using a 2048 image scan size with a 25 μs dwell time. False color chemical maps (Ca, Cr, Al, Si, Mg, Fe, Ti, S, P) were obtained at 1024 resolution using a 150 μs pixel dwell time and four frames, resulting in a total acquisition livetime of ~8 min. Spot analysis was performed on individual spinel, plagioclase, and olivine grains from PSA clasts C1-7 (to estimate olivine/spinel Mg#, plagioclase An#, and spinel Cr#) using a 20 s acquisition livetime, 1024 channels, and a process time of 4. Calibrations for EDS spot analyses were made using beam measurements on Cu-tape, and preset factory standards were used for quantitative analysis. For the PSA clasts, post-acquisition processing of the data set was applied to remove analyses with erroneous totals and cation sums. SEM-EDS data are provided in Figure S3, Data S2–S11.

Electron Probe Microanalysis

Chemical compositions of individual spinel, plagioclase, and olivine grains from three PSA clasts (clasts C5, C6, and C7) were obtained using a JEOL JXA-8200 electron
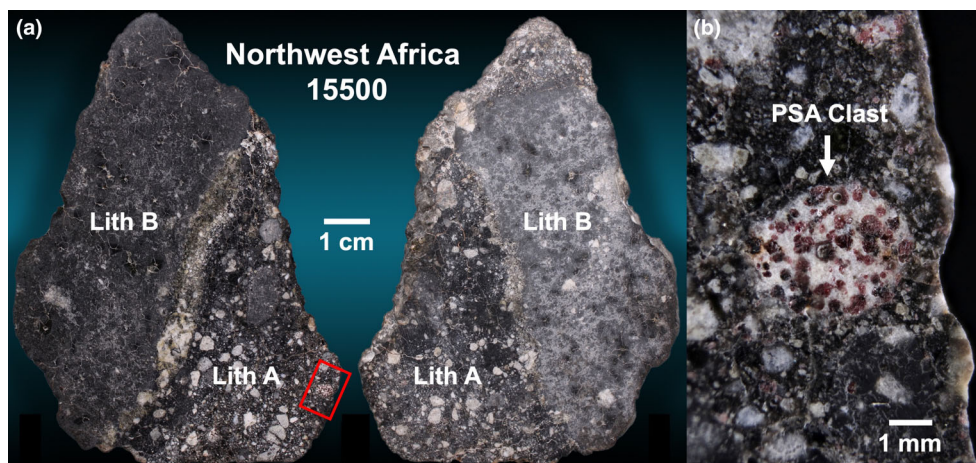
FIGURE 1. (a) Hand specimen image of NWA 15500 with lithologies A and B identified. (b) Close-up of pink spinel anorthosite (PSA) clast (location indicated by red box in part (a). (Color figure can be viewed at wileyonlinelibrary.com)

microprobe in the Department of Earth and Planetary Sciences at Washington University in St. Louis. The analytical conditions employed for this study included an accelerating voltage of 15 kV, a beam diameter of ~1 μm, and beam currents of 25 nA (for spinel and plagioclase from all PSA clasts, and olivine from PSA clast C6) and 100 nA (for olivine from PSA clasts C5 and C7). Element concentrations (Si, Ti, Al, Cr, Fe, Ni, Mn, Mg, Ca, Na, K, P, and S) were obtained using wavelength-dispersive spectrometry (WDS) with count times on peaks between 10 and 120 s and background intensities calculated using the mean atomic number background correction. Calibrations were made using a variety of natural and synthetic reference standards, yielding detection limits between 0.01 and 0.02 wt% for all oxides (SiO_2, TiO_2, Al_2O_3, Cr_2O_3, FeO, NiO, MnO, MgO, CaO, Na_2O, K_2O, P_2O_5, SO_3). Data reduction and matrix corrections were done using the Probe for EPMA software. EPMA data are provided in Data S1.

Inductively Coupled Plasma Mass Spectrometry

Representative fragments of NWA 15500 Lithologies A and B totaling ~175 mg each, and an ~100 mg PSA clast separate, were powdered using an agate mortar and pestle, of which ~45 mg from each respective powder was dissolved using HF, HNO_3, and HCL, and utilized for bulk chemical analysis of major, minor, and trace elements using a Thermo Fisher Scientific iCAP Qc ICP-MS in the Department of Earth and Planetary Sciences at Washington University in St. Louis. A solution from each of the dissolved samples was prepared at dilution factors of ~5000 (for minor and trace elements) and ~50,000 (for major elements) to achieve the necessary concentrations of each individual element in the range required for measurement in pulse counting mode. The solutions were measured multiple times at

both dilution factors to obtain average concentrations for each individual element (precision of the analysis for most elements using 1 SD of replicate analysis ranges from ~1% to 9%), and calibrations were made using dissolved USGS reference standards (BHVO-1, BCR-1, BIR-1, AGV-2) of known concentrations and dilution factors that match those of the sample. For most elements of interest, measurements of the reference standards (e.g., BHVO-1, BCR-1) were within ~1%–5% of previously reported values (Jochum et al., 2015). ICP-MS data are provided in Table S2.

RESULTS

Petrography and Mineral Chemistry

Northwest Africa 15500

Northwest Africa 15500 is a recently classified lunar meteorite (Gattacceca et al., 2023) that is brecciated and comprised of two distinct lithologies separated by a sharp contact (Figure 1). Our observations on the dichotomy between both lithologies in the sample were primarily assessed using thin section CML 1625-2 (Figure 2a).

Lithology (Lith) A is a polymict feldspathic fragmental breccia comprised of mm-sized, angular to sub-rounded lithic and mineral clasts set within a fine-grained matrix (Figure 2a–d). Lithic clasts identified in Lith A include, but are not limited to: anorthosites, noritic anorthosites, norites, olivine norites, troctolites, PSAs, and impact melt clasts; mineral clasts include isolated grains/fragments of plagioclase feldspar, olivine, pyroxene (both high-Ca and low-Ca varieties), and pink spinel. Given the polymict nature of Lith A, mineral phases display large compositional ranges: olivine $Fa_{17.8\pm12.1}$, range $Fa_{4.4-53.3}$, Fe/Mn = 85 ± 14, n = 76; low-Ca pyroxene $Fs_{23.9\pm13.8}$ $Wo_{3.4\pm1.2}$, range $Fs_{10.5-52.2}$ $Wo_{0.8-4.6}$,
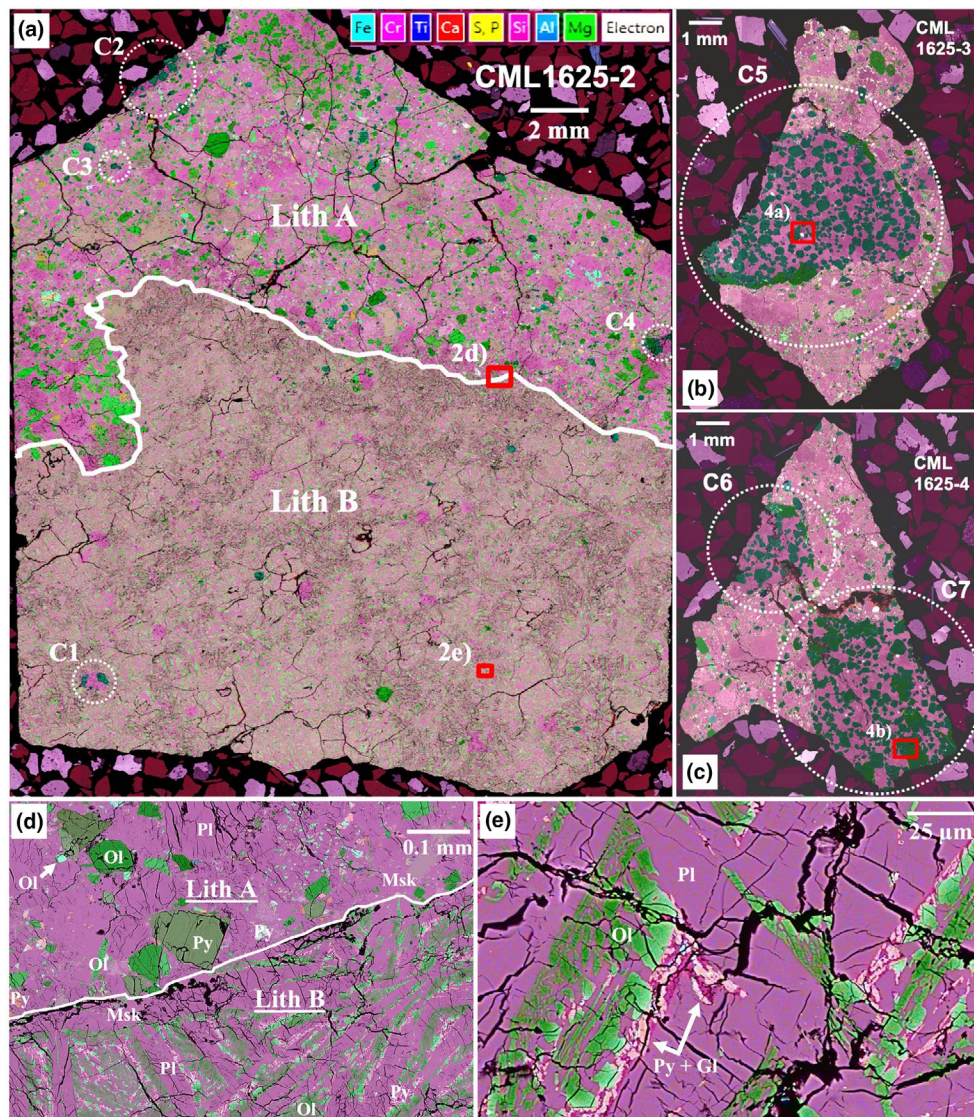
FIGURE 2. False color BSE + EDS mosaics of NWA 15500 thin sections (a) CML 1625-2, (b) CML 1625-3, and (c) CML 1625-4. Lithologies A (fragmental breccia) and B (clast-poor troctolitic impact melt rock) are identified in CML 1625-2; CML 1625-3; and CML 1625-4 contain only Lithology A. Areas in red boxes from CML 1625-3 and CML 1625-4 are shown in Figure 4a,b, respectively. PSA clasts C1-7 across all three thin sections are circled; close-up images of each PSA clast are shown in Figure 3. In this color combination, spinel appears blue-green, olivine as light to dark green, plagioclase or maskelynite as pink to purple, and pyroxene (not clearly visible due to small grain size) as green-gray to orange-tan. (d) Contact boundary between Lith A and B; (e) close-up of Lith B. Angular quartz and feldspar grains in epoxy used for thin section preparation in parts (a–c). Mineral phase abbreviations: Gl, glass; Msk, maskelynite; Ol, olivine; Pl, plagioclase feldspar; Py, pyroxene. (Color figure can be viewed at wileyonlinelibrary.com)

Mg# = 75.3 ± 14.3, Fe/Mn = 55 ± 8, n = 23; pigeonite $Fs_{33.0\pm10.1}$ $Wo_{10.7\pm3.3}$, range $Fs_{19.1-56.6}$ $Wo_{6.3-17.0}$, Mg# = 62.9 ± 11.5, Fe/Mn = 55 ± 7, n = 16; high-Ca pyroxene $Fs_{15.8\pm6.6}$ $Wo_{38.1\pm5.3}$, range $Fs_{5.8-29.6}$ $Wo_{26.0-45.7}$, Mg# = 74.6 ± 10.7, Fe/Mn = 50 ± 10, n = 15; calcic plagioclase An# = 96.5 ± 0.6, An# range = 94.9–98.0, n = 79 (where Fa = molar Fe/(Fe + Mg) × 100, Fs = molar Fe/(Fe + Mg + Ca) × 100, Wo = molar Ca/(Fe + Mg + Ca) x 100, Mg# = molar Mg/(Mg + Fe) × 100, An# = molar Ca/(Ca + Na) × 100, and non-range values represent mean ± 1 SD). Based on olivine and pyroxene Mg# and plagioclase An# (Papike et al., 1998), the sample is composed of both Mg-suite and FAN material, although the clast inventory is predominantly Mg-suite. Accessory phases identified in Lith A are scattered throughout the matrix and include ilmenite, merrillite, SiO_2-rich glass, troilite, and Fe-Ni metal.

Lith B represents a clast-poor troctolitic impact melt rock comprised primarily of compositionally zoned olivine dendrites (Av. grain diameter ~ 10 μm)
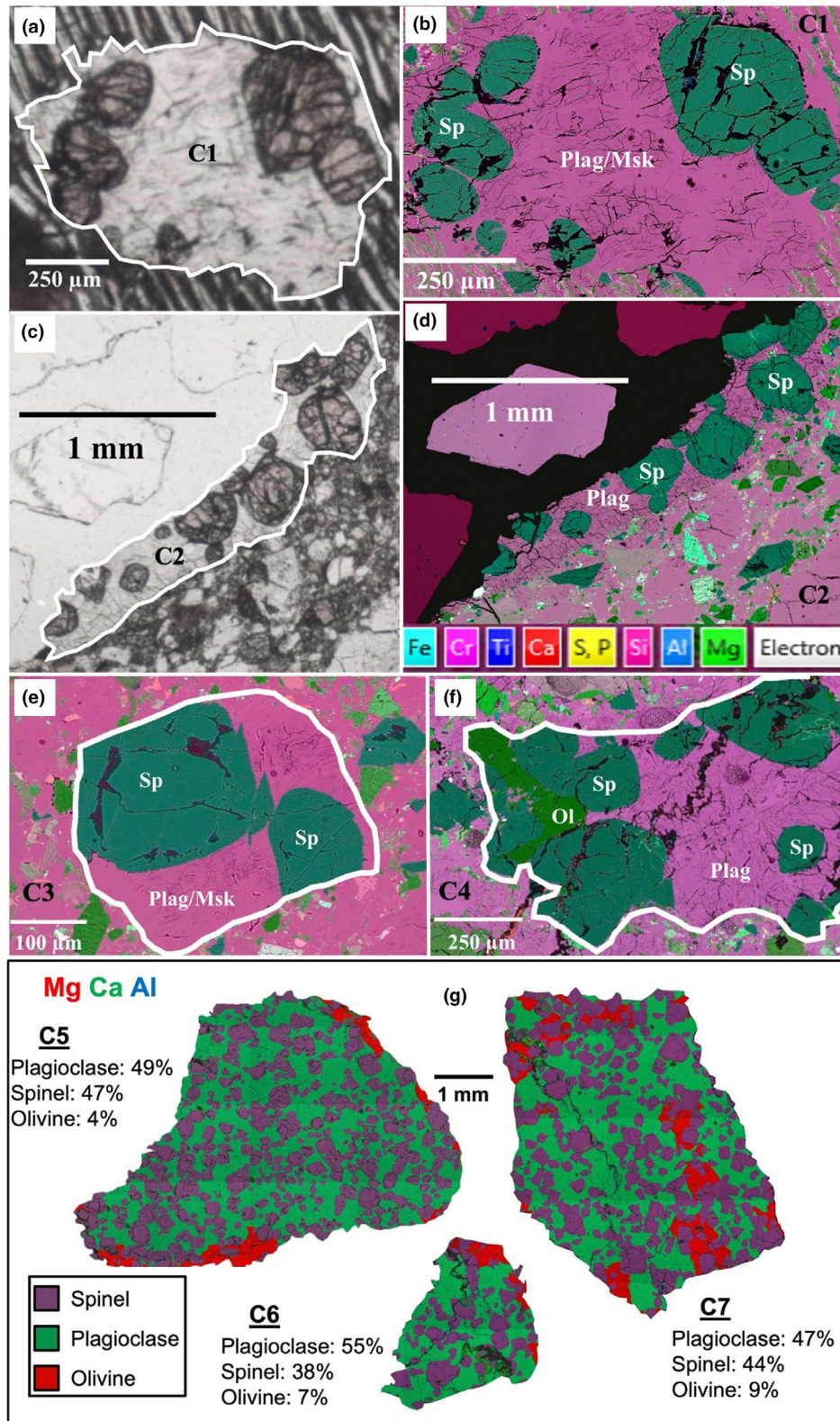
FIGURE 3. Transmitted plane-polarized light (PPL) images of PSA clasts C1-2 (a, c), and false color BSE + EDS images of PSA clasts C1-4 (b, d, e, f). Clasts outlined with mineral phases labeled (Msk, maskelynite; Ol, olivine; Plag, plagioclase; Sp, spinel). (g) False color RGB (Mg, Ca, Al) EDS images of PSA clasts C5-7; the color key for each mineral phase and its estimated modal abundance (in area %) within each clast are displayed. (Color figure can be viewed at wileyonlinelibrary.com)

($Fa_{21.6\pm5.8}$, range $Fa_{9.1-30.7}$, Fe/Mn = 79 ± 11, n = 35) set between unzoned laths of plagioclase feldspar (Av. grain diameter ~ 0.5 mm) (An# = 95.8 ± 0.8, An# range = 94.4–97.9, n = 40) (Figure 2d,e). Other phases identified in Lith B include intergrowths between zoned high-Ca pyroxene ($Fs_{27.4\pm12.9}$ $Wo_{39.5\pm2.7}$, range $Fs_{8.6-37.4}$ $Wo_{36.8-43.2}$, Mg# = 55.2 ± 20.5, Fe/Mn = 46 ± 5, n = 4) and Si-Al-rich glass that occur primarily when in contact with ferran olivine and plagioclase, isolated grains of unzoned low-Ca pyroxene ($Fs_{15.7\pm0.8}$ $Wo_{4.3\pm0.1}$, range $Fs_{15.2-16.3}$ $Wo_{4.3-4.4}$, Mg# = 83.6 ± 0.8, Fe/Mn = 57 ± 4, n = 2), and accessory ulvöspinel.

Olivine and pyroxene Fe/Mn ratios in both lithologies are consistent with NWA 15500 being lunar in origin (Karner et al., 2006; Papike et al., 2003). Plagioclase feldspar in both lithologies has been partially transformed into maskelynite, which appears smooth and lacks any noticeable fractures.

PSA Clasts

Pink spinel anorthosite clasts C1-7 from thin sections CML 1625-2, CML 1625-3, and CML 1625-4 are primarily observed within NWA 15500 Lith A, except for C1 from Lith B (Figure 2a–c). The PSA clasts are subrounded in appearance, ranging in size from ~0.4 mm to 6.8 mm when measured from the longest dimension, and in exposed area (i.e., surface area) from ~0.1 to ~20.1 mm^2 (Figure 3) (Table 1). They display coarse-grained, cumulate textures comprised of unzoned, irregularly fractured subhedral spinel grains (grain size range ~40–600 μm) poikilitically enclosed within unzoned plagioclase feldspar (some grains are fractured while others are smooth and partially transformed into maskelynite). Unzoned, irregularly fractured subhedral olivine grains are present in PSA clasts C4-7, most of which is observed to be poikilitically enclosing spinel along clast margins (Figures 3g and 4b). Mineral modes (in area %) estimated from PSA clasts C1-7 (Figure 3) using both visual inspection and ImageJ software are spinel (~36%–59%), plagioclase/maskelynite (~41%–64%), olivine (~0%–9%) (Table 1). Accessory opaque phases (<1%) observed in the PSA clasts include Ni-rich metal (molar Ni/Fe ratio ~0.7–1.2) and Ni-rich sulfide (molar Ni/S ratio ~0.2–0.7). In clast C5 (Figure 4a), Ni-rich sulfide appears to rim Ni-rich metal, and the entire assemblage is irregularly zoned in Ni.

There are differing opinions on whether lithic clasts in lunar samples can be representative of their protoliths (e.g., Gross, Treiman, & Mercer, 2014; Warren, 2012). Here, we infer that the large, exposed areas of the PSA clasts (~44.6 mm^2 combined), relative to the mineral grain size range in the PSA clasts (~40–600 μm), provide a representative sampling of the original PSA precursor lithology. Given that PSA clasts C5-7 are significantly larger than C1-4 in both size (~3.3–6.8 mm for C5-7, ~0.4–2.5 mm

for C1-4) and exposed area (~4.8–20.1 mm^2 for C5-7, ~0.1–0.8 mm^2 for C1-4), their modes (in area %) are probably more representative (38%–47% spinel, 47%–55% plagioclase/maskelynite, 4%–9% olivine). A weighted average of PSA C1-7 mineral modes (based on the relative proportion of exposed area for each PSA clast/combined exposed area) gives the best approximation of the modal mineralogy (in area %) of the PSA lithology in NWA 15500 (~45% spinel, ~49% plagioclase/maskelynite, ~6% olivine).

Major and minor element abundances of olivine, spinel, and plagioclase grains from PSA clasts C5-7 obtained using EPMA are listed in Table 2. For both major and minor elements, mineral phases (olivine, spinel, plagioclase) within each PSA clast appear relatively uniform in composition (with the exception being Al_2O_3 in olivine, although this may be the result of beam overlap). The abundances of minor elements Cr_2O_3, MnO, and NiO in olivine grains from the PSA clasts overlap with those of olivine grains from Mg-suite samples (Elardo et al., 2011; Shearer et al., 2015). While there are minor heterogeneities observed in olivine Mg# (molar Mg/(Mg + Fe) × 100), spinel Mg#, spinel Cr# (molar Cr/(Cr + Al) × 100), and plagioclase An# (molar Ca/(Ca + Na) × 100) between different PSA clasts (using EPMA data for C5-7 and SEM-EDS data for C1-7), it can be observed that our PSA clasts overlap with that of PST samples (Figure 5) (Prissel et al., 2016). Spinel and olivine grains within the same PSA clast are relatively compositionally uniform (Table 2). Application of the olivine–spinel Fe-Mg geothermometer (Jianping et al., 1995) to PSA clasts C4-7 yields an equilibration temperature range for the PSA clasts between 1107 and 1189°C, which overlaps with PST samples and plots near or just below the temperature for olivine and spinel that co-crystallized at magmatic temperatures (Figure 6) (Prissel et al., 2016). This suggests minor subsolidus re-equilibration for the PSA clasts.

A summary of the textural and geochemical parameters observed in PSA clasts C1-7 that are described here are listed in Table 1. Despite what appears to be an apparent systematic variation in spinel Cr# between data collected by EPMA versus SEM-EDS (e.g., PSA C5 spinel Cr# ~3.7 from EPMA and ~4.0 from SEM-EDS), in general, there is substantial overlap between the mineral chemical data collected on PSA clasts using EPMA (for C5-7) with that of SEM-EDS (for C1-7) (Figures 5 and 6). Combining all data, PSA clasts have spinel Mg# ~81–88, Cr# ~3.6–4.1, olivine Mg# ~91–93, and plagioclase/maskelynite An# ~95–97.

Bulk Chemistry

The major, minor, and trace element abundances obtained from representative bulk rock samples of NWA

TABLE 1. Textural and geochemical parameters observed in PSA clasts C1-7.

	PSA C1	PSA C2	PSA C3	PSA C4	PSA C5	PSA C6	PSA C7	Combined*
Thin section ID	CML 1625-2	CML 1625-2	CML 1625-2	CML 1625-2	CML 1625-3	CML 1625-4	CML 1625-4	
Clast length (mm) (longest dimension)	~1.1	~2.5	~0.4	~1.2	~6.8	~3.3	~6.5	~44.6
Clast exposed area (mm²)	~0.7	~0.8	~0.1	~0.6	~20.1	~4.8	~17.5	Combined*
Mineral modes (area %)	Sp: 36 Pl/Msk: 64 Ol: 0	Sp: 51 Pl/Msk: 49 Ol: 0	Sp: 59 Pl/Msk: 41 Ol: 0	Sp: 43 Pl/Msk: 52 Ol: 5	Sp: 47 Pl/Msk: 49 Ol: 4	Sp: 38 Pl/Msk: 55 Ol: 7	Sp: 44 Pl/Msk: 47 Ol: 9	Weighted Average* Sp: 45 Pl/Msk: 49 Ol: 6
Olivine Mg#				*92.3 ± 0.1* *n = 3*	**91.2 ± 0.3** **n = 17** *91.8 ± 0.3* *n = 13*	**91.0 ± 0.2** **n = 7** *91.6 ± 0.1* *n = 5*	**93.0 ± 0.2** **n = 22** *92.8 ± 0.1* *n = 4*	
Spinel Mg#	*81.3 ± 0.3* *n = 5*	*85.1 ± 1.1* *n = 16*	*86.6 ± 0.1* *n = 10*	*86.7 ± 0.3* *n = 7*	**85.0 ± 0.3** **n = 23** *84.8 ± 0.6* *n = 41*	**84.7 ± 0.4** **n = 12** *84.1 ± 0.6* *n = 13*	**87.7 ± 0.3** **n = 24** *87.3 ± 0.3* *n = 13*	
Spinel Cr#	*3.9 ± 0.1* *n = 5*	*4.0 ± 0.1* *n = 16*	*3.9 ± 0.1* *n = 10*	*3.9 ± 0.1* *n = 7*	**3.7 ± 0.1** **n = 23** *4.0 ± 0.1* *n = 41*	**3.8 ± 0.1** **n = 12** *4.1 ± 0.1* *n = 13*	**3.6 ± 0.1** **n = 24** *3.9 ± 0.1* *n = 13*	
Plagioclase An#	*95.1 ± 0.4* *n = 13*	*96.2 ± 0.4* *n = 13*	*97.0 ± 0.2* *n = 8*	*96.7 ± 0.2* *n = 7*	**95.9 ± 0.3** **n = 22** *96.2 ± 0.3* *n = 41*	**95.7 ± 0.4** **n = 14** *95.6 ± 0.3* *n = 11*	**96.9 ± 0.2** **n = 22** *97.0 ± 0.5* *n = 11*	
Ol-Sp Fe-Mg Kd				*~1.83*	**~1.83** *~1.77*	**~1.83** *~1.82*	**~1.87** *~1.88*	
Ol-Sp Fe-Mg equilibration temperature (°C)				*~1139*	**~1136** *~1189*	**~1143** *~1152*	**~1109** *~1107*	

Note: Mg# = molar Mg/(Mg + Fe) × 100, Cr# = molar Cr/(Cr + Al) × 100, An# = molar Ca/(Ca + Na) × 100, Ol-Sp Fe-Mg Kd value and equilibration temperature from Jianping et al. (1995). Values obtained using EPMA data in bold and SEM-EDS data in italics. *n* = number of analyses. Asterisk (*) denotes combined exposed area for PSA C1-7, and weighted average estimate (based on the relative proportion of exposed area for each PSA clast/combined area) of the modal mineralogy for the PSA lithology.
Abbreviations: Msk, maskelynite; Ol, olivine; Pl, plagioclase; Sp, spinel.
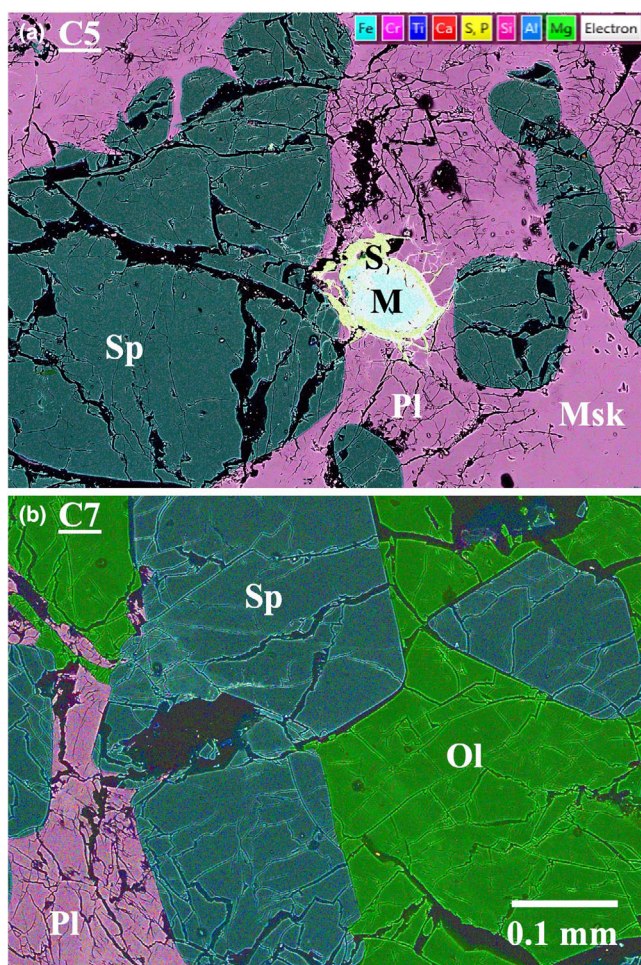
FIGURE 4. False color BSE + EDS images of PSA clasts (a) C5 and (b) C7. Mineral phase abbreviations: M, Ni-rich metal; Msk, maskelynite; Ol, olivine; Pl, plagioclase feldspar; S, Ni-rich sulfide; Sp, spinel. Phase colors as in Figures 2 and 3. (Color figure can be viewed at wileyonlinelibrary.com)

15500 Lithologies A and B, and a PSA clast separate, are displayed in Table 3.

Northwest Africa 15500

The bulk compositions of NWA 15500 Lith A and Lith B are nearly identical for a variety of major, minor, and trace elements (Table 3). Incompatible element abundances (e.g., Sm, Th) for both Lith A and Lith B plot within the range observed in lunar meteorites and are compositionally similar to average Feldspathic Highlands Terrane (FHT) (Figure 7) (Jolliff et al., 2000; Korotev, 2005; Korotev & Irving, 2021). This is consistent with the lithic clast inventory in NWA 15500 being primarily feldspathic. Rare earth element (REE) abundances for Lith A and Lith B plot within the range of olivine-bearing Mg-suite samples (Papike et al., 1998) (Figure 8); the REE patterns are similar to, but somewhat lower in abundance than, that of average highland meteorites

(Cahill et al., 2004). The CI-normalized spider diagram patterns for NWA 15500 Lith A and Lith B are essentially identical for most elements (Figure 9a), and plot between bulk compositions of average FAN and Mg-suite samples (Cahill et al., 2004) (Figure 9b), similar to average highland meteorites.

PSA Clast

Given that there is relatively limited variability in both modal mineralogy and mineral major/minor element abundances between "likely more intact" mm-sized PSA clasts (e.g., C5-7) that are more representative of PSA as a whole than smaller clasts (e.g., C1-4, Table 1), and that the ~100 mg powder was derived from a representative mm-sized PSA clast precursor, it can be assumed here that the bulk composition of the PSA clast separate is largely representative of a homogeneous population of PSA material.

The bulk composition of the PSA clast separate displays REE abundances that overlap with the range for Apollo FANs (Floss et al., 1998; Papike et al., 1998) (Figure 8). Significantly, the PSA clast is depleted in REEs relative to PST and olivine-bearing Mg-suite samples, and displays a more prominent Eu-anomaly than PST or olivine-bearing Mg-suite, more similar to Apollo FANs (Figure 8).

The PSA clast separate displays noticeable enrichments in V, Cr, Co, and Ni compared with the Lith A and Lith B hosts (Figure 9a). This is due to the compositional influence of pink spinel (enriched in V and Cr) and Ni-rich metal (enriched in Co and Ni) found within the PSA clasts. This effect can also explain slight enrichments in Lith A relative to Lith B in V, Cr, Co, and Ni, as PSA clasts are predominantly found in Lith A. Compared with PST samples on the spider diagram (Figure 9c), the PSA clast displays similar abundances of major/minor mafic elements such as Mg, Ca, Si, Cr, Mn, and Fe, but is relatively depleted in incompatible trace elements such as Sr, Ba, Sc, Hf, Ta, and Th. Compared with average FAN, there is a close match to PSA in Ba; however Sr, Sc, Hf, and Th abundances are relatively higher in average FAN than in PSA (Figure 9c). Despite being at a comparable Mg# (~84.7), the Sc/Sm (~20.5) and Ti/Sm (~7240) ratios of the PSA clast separate are both noticeably higher than that reported in PST and Mg-suite samples (Ma et al., 1981; Papike et al., 1998; Shearer et al., 2015), and instead overlap with the range reported in Apollo FANs (Cahill et al., 2004; Papike et al., 1998; Shearer et al., 2015).

As the Ni and Co abundances of the PSA clast separate are primarily derived from Ni-rich metal grains, the bulk Ni/Co ratio provides a good proxy for the average Ni/Co ratio of the Ni-rich metal grains. Here, the average Ni/Co ratio of the Ni-rich metal grains from

TABLE 2. Averaged major and minor element EPMA mineral compositions for olivine, spinel, and plagioclase grains in PSA clasts C5-7.

Oxide (wt%)	Olivine			Spinel			Plagioclase		
	PSA clast 5 (n = 17)	PSA clast 6 (n = 7)	PSA clast 7 (n = 22)	PSA clast 5 (n = 23)	PSA clast 6 (n = 12)	PSA clast 7 (n = 24)	PSA clast 5 (n = 22)	PSA clast 6 (n = 14)	PSA clast 7 (n = 22)
SiO_2	41.94 ± 0.11	40.91 ± 0.17	42.19 ± 0.12	n.d.	n.d.	n.d.	43.68 ± 0.14	43.69 ± 0.25	43.57 ± 0.26
TiO_2	0.05 ± 0.01	0.05 ± 0.02	0.03 ± 0.01	0.12 ± 0.02	0.17 ± 0.03	0.08 ± 0.01	0.01 ± 0.01	0.01 ± 0.01	0.01 ± 0.01
Al_2O_3	0.05 ± 0.05	0.08 ± 0.12	0.08 ± 0.08	66.76 ± 0.38	66.55 ± 0.31	67.36 ± 0.25	36.44 ± 0.14	36.32 ± 0.19	36.63 ± 0.14
Cr_2O_3	0.02 ± 0.02	0.01 ± 0.01	0.02 ± 0.01	3.84 ± 0.11	3.89 ± 0.12	3.71 ± 0.10	n.d.	n.d.	n.d.
FeO	8.77 ± 0.31	8.74 ± 0.15	7.04 ± 0.16	7.13 ± 0.17	7.23 ± 0.17	5.85 ± 0.16	0.04 ± 0.02	0.03 ± 0.03	0.03 ± 0.01
NiO	0.01 ± 0.01	0.02 ± 0.06	0.02 ± 0.01	0.01 ± 0.01	n.d.	0.01 ± 0.01	n.d.	n.d.	n.d.
MnO	0.12 ± 0.01	0.13 ± 0.02	0.09 ± 0.01	0.07 ± 0.02	0.08 ± 0.01	0.05 ± 0.01	0.01 ± 0.01	0.01 ± 0.02	0.01 ± 0.01
MgO	51.31 ± 0.33	49.41 ± 0.26	52.52 ± 0.24	22.74 ± 0.17	22.39 ± 0.17	23.41 ± 0.13	0.08 ± 0.01	0.08 ± 0.01	0.12 ± 0.03
CaO	0.03 ± 0.02	0.04 ± 0.04	0.04 ± 0.02	n.d.	n.d.	n.d.	19.33 ± 0.14	19.14 ± 0.16	19.41 ± 0.16
Na_2O	n.d.	n.d.	n.d.	n.d.	n.d.	n.d.	0.46 ± 0.03	0.48 ± 0.04	0.34 ± 0.02
K_2O	n.d.	n.d.	n.d.	n.d.	n.d.	n.d.	n.d.	n.d.	n.d.
P_2O_5	n.d.	n.d.	n.d.	n.d.	n.d.	n.d.	n.d.	n.d.	n.d.
SO_3	n.d.	n.d.	n.d.	n.d.	n.d.	n.d.	n.d.	n.d.	n.d.
Total	102.26 ± 0.18	99.40 ± 0.29	102.02 ± 0.22	100.64 ± 0.59	100.30 ± 0.31	100.46 ± 0.27	100.05 ± 0.25	99.76 ± 0.30	100.13 ± 0.44
Cation sum	3.000 ± 0.001 (4 O)	2.994 ± 0.002 (4 O)	2.999 ± 0.002 (4 O)	2.993 ± 0.001 (4 O)	2.990 ± 0.001 (4 O)	2.991 ± 0.001 (4 O)	5.009 ± 0.003 (8 O)	5.007 ± 0.003 (8 O)	5.006 ± 0.003 (8 O)
Mg#	91.2 ± 0.3	91.0 ± 0.2	93.0 ± 0.2	85.0 ± 0.3	84.7 ± 0.4	87.7 ± 0.3			
Cr#				3.7 ± 0.1	3.8 ± 0.1	3.6 ± 0.1			
An#							95.9 ± 0.3	95.7 ± 0.4	96.9 ± 0.2

Note: Cation sums for olivine/spinel calculated using four oxygen; cation sums for plagioclase calculated using eight oxygen. ± is listed as 1σ SD.
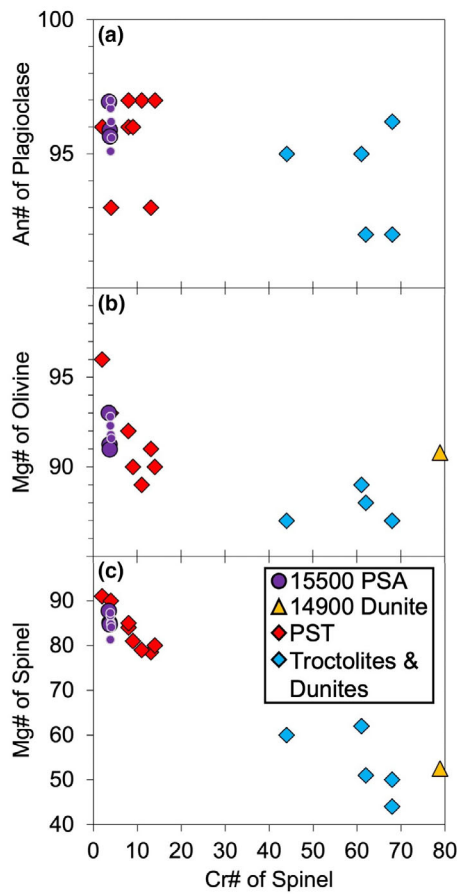Abbreviations: *n*, number of analyses; n.d., not detected.

FIGURE 5. Plot of spinel Cr# against (a) plagioclase An#, (b) olivine Mg#, and (c) spinel Mg# for NWA 15500 PSA clasts C1-7 (SEM-EDS data, smaller symbols) and C5-7 (EPMA data, larger symbols). Also included are Mg-suite troctolites, dunites, and PST (Prissel et al., 2016, and references listed therein), and the dunite clast from NWA 14900 (Sheikh et al., 2022). Symbol sizes largely encompass chemical variations observed within each PSA clast. EPMA and SEM-EDS data collected from the same PSA clast are largely in agreement. Figure modified after Prissel et al. (2016). (Color figure can be viewed at wileyonlinelibrary.com)

the PSA clast separate (Ni/Co ~25) plots within the range of Ni/Co ratios measured from exogenous metal grains in lunar samples that were derived from impactor contamination (Day, 2020).

DISCUSSION

Genetic Relationship Between NWA 15500 PSA and Mg-Suite PST

We suggest a genetic relationship between the PSA clasts in NWA 15500 and PST clasts in Apollo Mg-suite samples based on (1) texture and mineralogy, (2) major/minor element mineral compositions, and (3) bulk major/minor element abundances. For textures and mineralogy, the poikilitic texture observed between spinel
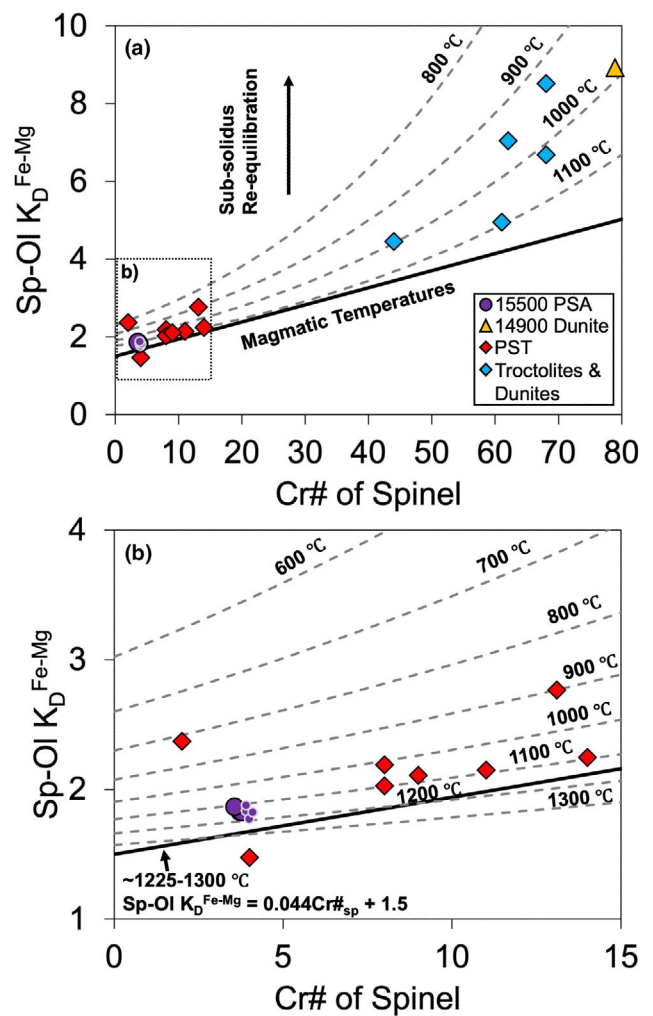

FIGURE 6. (a) Plot of spinel Cr# against Sp-Ol K_D^{Fe-Mg} (spinel molar Fe/Mg ratio × olivine molar Mg/Fe ratio) for NWA 15500 PSA clasts C4-7 (SEM-EDS data, smaller symbols) and C5-7 (EPMA data, larger symbols). Also included are Mg-suite troctolites, dunites, and PST (Prissel et al., 2016, and references listed therein), and the dunite clast from NWA 14900 (Sheikh et al., 2022). Isotherms are derived using the olivine-spinel Fe-Mg geothermometer equation of Jianping et al. (1995). Bold line represents the equilibrium line between olivine and spinel at magmatic temperatures (Prissel et al., 2016), deviations from this line are noted by the arrow as being due to subsolidus re-equilibration. Symbol sizes largely encompass chemical variations observed within each PSA clast. EPMA and SEM-EDS data collected from the same PSA clast are largely in agreement. (b) Inset provides a more detailed view of PSA in comparison with PST. Figure modified after Prissel et al. (2016). Thermometry calculations for PSA clasts and isotherms are provided in Data S1 and Data S8–S11 for PSA clasts, Table S1 for isotherms). (Color figure can be viewed at wileyonlinelibrary.com)

chadacrysts and plagioclase oikocrysts in the PSA clasts, the grain sizes/shapes of spinel, the partial amorphization of plagioclase to maskelynite, and the presence of metal and sulfide are all similarly observed in PST clasts (Bence

TABLE 3. Major, minor, and trace element ICP-MS bulk rock compositions for NWA 15500 Lith A, Lith B, and a PSA clast separate.

	NWA 15500 Lith A	NWA 15500 Lith B	NWA 15500 PSA
Oxide (wt%)			
SiO₂*	43.13	45.81	34.62
TiO₂	0.25 ± 0.003	0.30 ± 0.0003	0.09 ± 0.001
Al₂O₃	24.62 ± 0.04	22.39 ± 0.35	37.67 ± 1.61
Cr₂O₃	0.29 ± 0.004	0.10 ± 0.001	1.14 ± 0.01
FeO	5.79 ± 0.02	5.93 ± 0.04	4.97 ± 0.11
NiO	0.03 ± 0.0003	0.01 ± 0.0001	0.24 ± 0.002
MnO	0.07 ± 0.001	0.07 ± 0.001	0.04 ± 0.001
MgO	13.40 ± 0.13	11.83 ± 0.06	15.47 ± 1.04
CaO	11.97 ± 0.07	13.07 ± 0.26	5.54 ± 0.09
Na₂O	0.35 ± 0.001	0.38 ± 0.0004	0.19 ± 0.004
K₂O	0.04 ± 0.001	0.03 ± 0.0003	0.02 ± 0.001
P₂O₅	0.06 ± 0.01	0.07 ± 0.003	0.02 ± 0.004
Element (ppm)			
Li	4.14 ± 0.96	4.29 ± 0.41	2.11 ± 0.25
Sc	6.78 ± 0.41	7.87 ± 0.10	1.45 ± 0.07
V	36.17 ± 0.32	20.72 ± 0.22	124.30 ± 1.33
Co	22.53 ± 0.22	17.70 ± 0.20	77.99 ± 1.22
Cu	4.63 ± 0.11	3.55 ± 0.0001	4.89 ± 0.05
Zn	18.73 ± 0.92	8.02 ± 0.14	8.97 ± 0.20
Ga	3.27 ± 0.02	2.25 ± 0.02	4.28 ± 0.22
Rb	0.64 ± 0.03	0.37 ± 0.05	0.16 ± 0.02
Sr	133.39 ± 2.18	137.24 ± 4.26	71.02 ± 0.04
Y	6.45 ± 0.02	5.95 ± 0.10	0.46 ± 0.02
Zr	20.68 ± 0.04	18.50 ± 0.62	1.21 ± 0.01
Nb	1.37 ± 0.03	1.27 ± 0.02	0.11 ± 0.01
Ba	32.79 ± 0.70	26.76 ± 0.01	7.83 ± 0.09
La	1.732 ± 0.007	1.393 ± 0.012	0.205 ± 0.005
Ce	4.378 ± 0.035	3.512 ± 0.056	0.490 ± 0.006
Pr	0.542 ± 0.009	0.480 ± 0.014	0.055 ± 0.002
Nd	2.683 ± 0.007	2.354 ± 0.070	0.267 ± 0.023
Sm	0.779 ± 0.032	0.690 ± 0.023	0.071 ± 0.002
Eu	0.635 ± 0.020	0.704 ± 0.013	0.334 ± 0.005
Gd	0.948 ± 0.027	0.885 ± 0.043	0.086 ± 0.010
Tb	0.174 ± 0.0002	0.159 ± 0.0003	0.014 ± 0.001
Dy	1.119 ± 0.003	1.031 ± 0.011	0.077 ± 0.007
Ho	0.233 ± 0.001	0.221 ± 0.004	0.018 ± 0.002
Er	0.685 ± 0.005	0.643 ± 0.013	0.050 ± 0.003
Tm	0.110 ± 0.004	0.103 ± 0.0002	0.007 ± 0.0004
Yb	0.670 ± 0.016	0.631 ± 0.029	0.058 ± 0.002
Lu	0.094 ± 0.002	0.090 ± 0.001	0.009 ± 0.001
Hf	0.543 ± 0.003	0.490 ± 0.026	0.033 ± 0.006
Ta	0.072 ± 0.005	0.071 ± 0.004	0.006 ± 0.001
W	0.100 ± 0.004	0.736 ± 0.076	0.078 ± 0.013
Tl	0.208 ± 0.020	0.164 ± 0.018	0.181 ± 0.026
Pb	3.067 ± 0.011	0.282 ± 0.010	1.004 ± 0.019
Th	0.225 ± 0.005	0.174 ± 0.008	0.014 ± 0.0003
U	0.082 ± 0.002	0.077 ± 0.006	0.013 ± 0.001
Mg#	80.5	78.0	84.7

Note: Major and minor elements are reported in wt% oxide, trace elements are reported in ppm. SiO₂ abundance (SiO₂*) estimated by subtracting other oxide abundances from 100. ± is listed as 1σ SD of replicate analyses.

Abbreviation: n.d., not detected.

et al., 1975; Blanchard et al., 1976, 1977; Ma et al., 1981; Neal and Taylor, 1998; Papike et al., 1998; Shearer et al., 2015), although PSA contains a greater modal abundance of spinel and lesser abundance of olivine. For mineral compositions, the Mg# of olivine, Mg# of spinel, Cr# of spinel, and An# of plagioclase all overlap between PSA and PST (Figure 5), and Cr_2O_3, MnO, and NiO contents of olivine (Table 2), and the high Ni content of metal and sulfide, are also similar (Bence et al., 1975; Blanchard et al., 1976, 1977; Ma et al., 1981; Neal and Taylor, 1998; Papike et al., 1998; Shearer et al., 2015; Prissel et al., 2016). For bulk abundances, the PSA clast separate we analyzed chemically resembles PST clasts (Blanchard et al., 1976; Ma et al., 1981; Neal and Taylor, 1998; Papike et al., 1998) for elements concentrated in mafic minerals (Mg, Ca, Si, Cr, Mn, Fe, Sc, V, Co, and Ni) and for some elements concentrated in feldspar (Al, Na, and K) (Figure 9c). However, the abundances for other incompatible elements (Ba, Ti, Zr, Ta, Th) differ between PST and PSA, with lower abundances in PSA (Figure 9c). In summary, the NWA 15500 PSA data not only suggest a genetic link between PSA and PST but also indicate that incompatible element abundances are lower in PSA compared to Apollo PST.

It has been well established on the basis of texture, mineral chemistry (e.g., olivine Cr_2O_3, NiO, MnO, plagioclase An#) and bulk composition (e.g., Sc/Sm, Ti/Sm ratios) that the PST represent a member of the lunar highlands magnesian suite (Mg-suite) (Ma et al., 1981; Papike et al., 1998; Ryder, 1991; Shearer et al., 2015; Warren & Wasson, 1980). Unlike other Mg-suite lithologies (e.g., norites, dunites, troctolites), however, the high olivine Mg# (>88) (Prissel et al., 2016) and presence of minor pink spinel (~5–6 vol%) in PST samples (Gross, Isaacson, et al., 2014) requires a model for the petrogenesis of PST that (1) facilitates the crystallization of Mg-Al spinel and (2) delays the crystallization of olivine, which would act to lower the bulk Mg# of the system (Prissel et al., 2016; Prissel & Gross, 2020). Therefore, the primary model for the formation of PST has been suggested to invoke minor crustal assimilation of anorthositic crust into an Mg-suite parental magma at depth (Papike et al., 1998; Prissel et al., 2016; Prissel & Gross, 2020; Ryder, 1991; Shearer et al., 2015; Warren & Wasson, 1980).

We suggest here that PSA could have formed by magma–wallrock interactions between plagioclase-undersaturated Mg-suite parental melts and anorthositic crust, and that an increased degree of crustal assimilation is required for PSA relative to PST for a given Mg-suite parental melt (in agreement with the models of Chen et al., 2023; Prissel & Gross, 2020; Prissel et al., 2014, 2016). Although enthalpy constraints have been used to argue against the formation of PSA by magma–wallrock
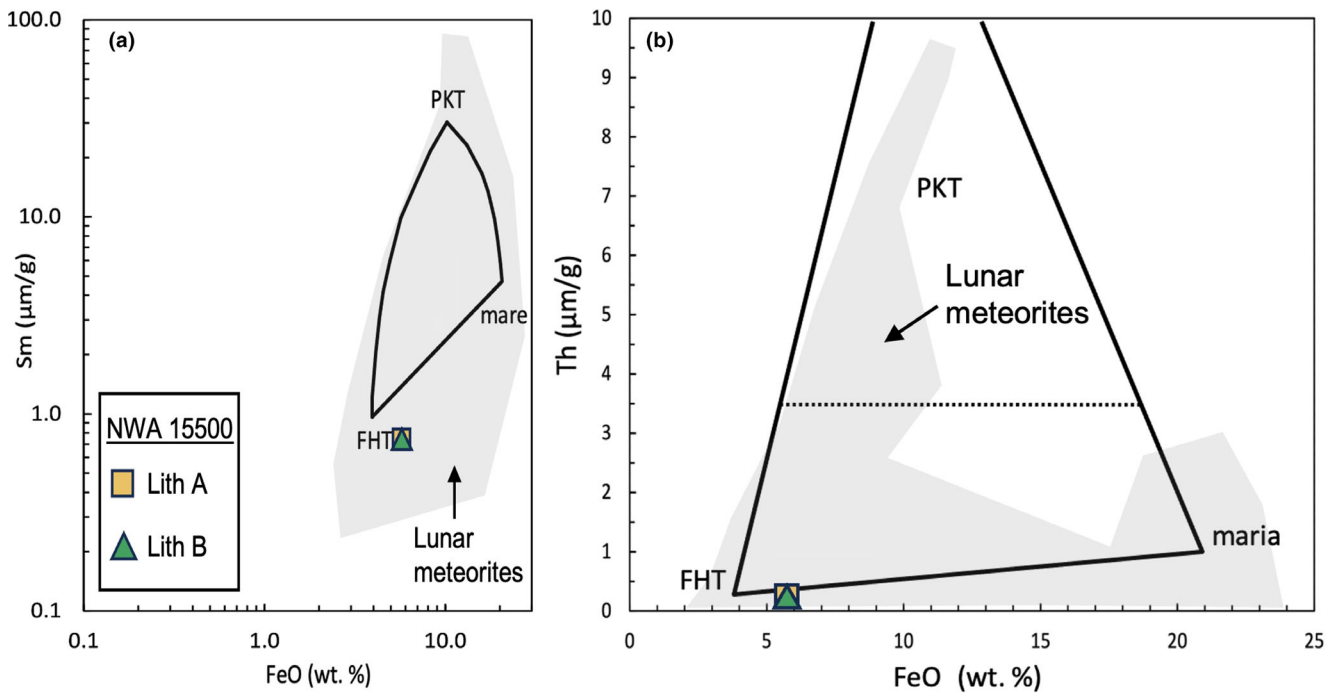
FIGURE 7. Plot of FeO (wt%) against (a) Sm (ppm) and (b) Th (ppm) for bulk compositions of NWA 15500 lithologies A and B. Also included is the shaded region where lunar meteorites plot, and the mixing triangle between Feldspathic Highlands Terrane (FHT), Procellarum KREEP Terrane (PKT), and lunar maria/mare. The dotted line in (b) separates PKT (above) from non-PKT. Figure modified after Korotev and Irving (2021). (Color figure can be viewed at wileyonlinelibrary.com)

interactions (Treiman et al., 2019), the small amount of PST in the Mg-suite troctolite collection (~2% by mass, Prissel & Gross, 2020), and the still smaller amount of PSA, might indicate that magma–wallrock interactions could have operated on a local scale in the lunar interior.

There are at least two possibilities that could explain the depletion in bulk incompatible lithophile trace element abundances (REEs, Sr, Ba, Sc, Hf, Ta, Th) for PSA relative to PST (and to FAN in some cases). The first is that PST and PSA represent different stages in a crustal assimilation process, with PSA representing a more advanced stage. If PST represents the onset of assimilation-type processes of anorthositic crust, partial melting of a relatively minor fraction of anorthositic wallrock (rather than complete assimilation) would lead to slight enrichments in incompatible elements for the PST REE-pattern, whereas continued assimilation of a more "depleted" wallrock component (at a larger fraction) into the Mg-suite parental melt (potentially due to either later recharge or a higher initial melt/wallrock temperature) would result in a dilution of the REE signature and relative depletion of incompatible elements (Heinonen et al., 2021). This could explain why PSA is relatively depleted in Sc and Ti compared to PST (Figure 9c), yet unlike PST, PSA has FAN-like Ti/Sm and Sc/Sm ratios (Cahill et al., 2004; Papike et al., 1998; Shearer

et al., 2015). However, this would assume that PST and PSA formed from the same Mg-suite parental melt and/or the same magma chamber, which may not be the case. For example, application of a simple binary mixing approach between an average PST and average FAN to produce a PSA-like REE pattern would require a 90% FAN component, which seems implausible given that it requires more "mass" of wallrock than Mg-suite parental melt.

The second possibility is that PSA and PST formed in different geochemical systems. Given that PST samples display an incompatible element enrichment relative to PSA, it might be possible that the parental Mg-suite melt for PST inherited a slight KREEP component to it, which would be plausible given that Apollo PST samples were recovered on the nearside close to the PKT. As NWA 15500 is depleted in incompatible elements relative to the PKT (Korotev, 2005; Korotev & Irving, 2021), this indicates that NWA 15500 (and the PSA clasts in it) must have been derived away from the PKT, most likely from the lunar farside. On a broader scale, if PSA formed on the lunar farside, this would support models calling for a Moon-wide distribution of Mg-suite magmatism (Prissel et al., 2014), and by extension, would imply that PKT materials (e.g., KREEP) were not a necessary ingredient in producing PSA and other Mg-suite rocks.
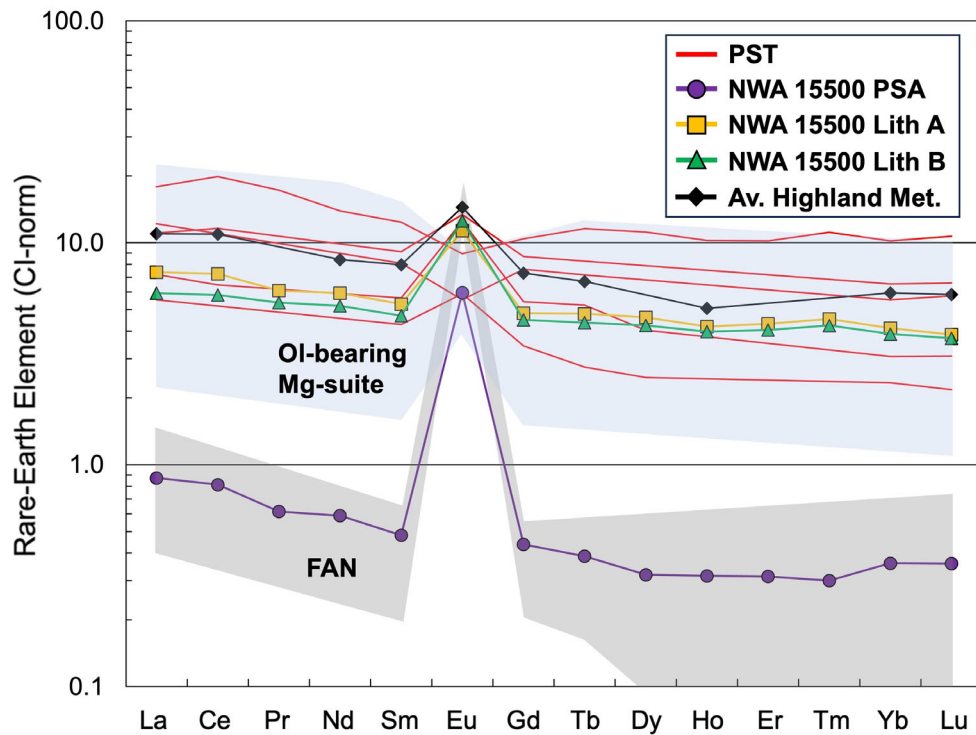
FIGURE 8. CI-normalized REE diagram (CI-chondrite abundances from Anders and Grevesse, 1989) for bulk compositions of NWA 15500 Lith A, Lith B, and a PSA clast separate. Also plotted are REE patterns for various Apollo PST samples (Bence et al., 1975; Blanchard et al., 1976, 1977; Ma et al., 1981; Neal & Taylor, 1998; Papike et al., 1998), and for the average composition of lunar highland meteorites (Cahill et al., 2004). Shaded fields are for Apollo FANs (Floss et al., 1998; Papike et al., 1998) and Apollo olivine (Ol)-bearing Mg-suite samples (troctolitic anorthosite and troctolite data from Papike et al., 1998). Where applicable, Gd values for PST samples and samples that outline the shaded FAN and Ol-bearing Mg-suite fields were interpolated using the equation $Gd* = (Sm \times Tb)^{1/2}$. (Color figure can be viewed at wileyonlinelibrary.com)

Given the complexities of assimilation processes within a dynamic environment such as a crystallizing magma chamber (Heinonen et al., 2021), further geochemical modeling work is needed to properly constrain the temporal/spatial genetic relationship between PSA and PST. In addition, more trace element data for PSA clasts are needed to help inform such modeling.

Genetic Relationship Between NWA 15500 PSA and M³ PSA

Despite the modal mineralogical constraints of NWA 15500 PSA clasts matching those of estimates for the PSA lithology from M³ remote sensing data (spinel-rich, <5 vol% olivine/pyroxene, Pieters et al., 2011), there is a slight compositional difference in the Mg# of spinel between NWA 15500 PSA (Mg# ~81.3–87.7, Table 1) and PSA estimated from M³ (Mg# >88) (Figure 10) (Jackson et al., 2014). Below, we evaluate three potential scenarios that can account for this discrepancy, and our justification for why NWA 15500 PSA likely represents

the best "ground truth" candidate in our lunar sample collection of M³ PSA.

In scenario one (Figure 10a), the difference in spinel Mg# between NWA 15500 PSA and M³ PSA can be attributed to variations in the Mg# between candidate Mg-suite parental melts. This can originate from several factors. For example, an increasing degree of olivine fractionation either during ascent or prior to the onset of assimilation will result in an Mg-suite parental melt (and resulting spinel composition) that is relatively depleted in Mg# (Prissel et al., 2016; Prissel & Gross, 2020). Alternatively, due to the range in olivine Mg# from early formed LMO cumulates (Elkins-Tanton et al., 2011; Schmidt & Kraettli, 2022), partial melting of an olivine-rich LMO cumulate with a lower Mg# would also result in an Mg-suite parental melt with lower Mg#. The lack of significant overlap in Th abundances between either NWA 15500 Lith A or NWA 15500 PSA with that of Mg-spinel-rich exposures observed by remote sensing (Pieters et al., 2014), in combination with the slight compositional difference in spinel Mg# between NWA 15500 PSA clasts and the estimated PSA composition
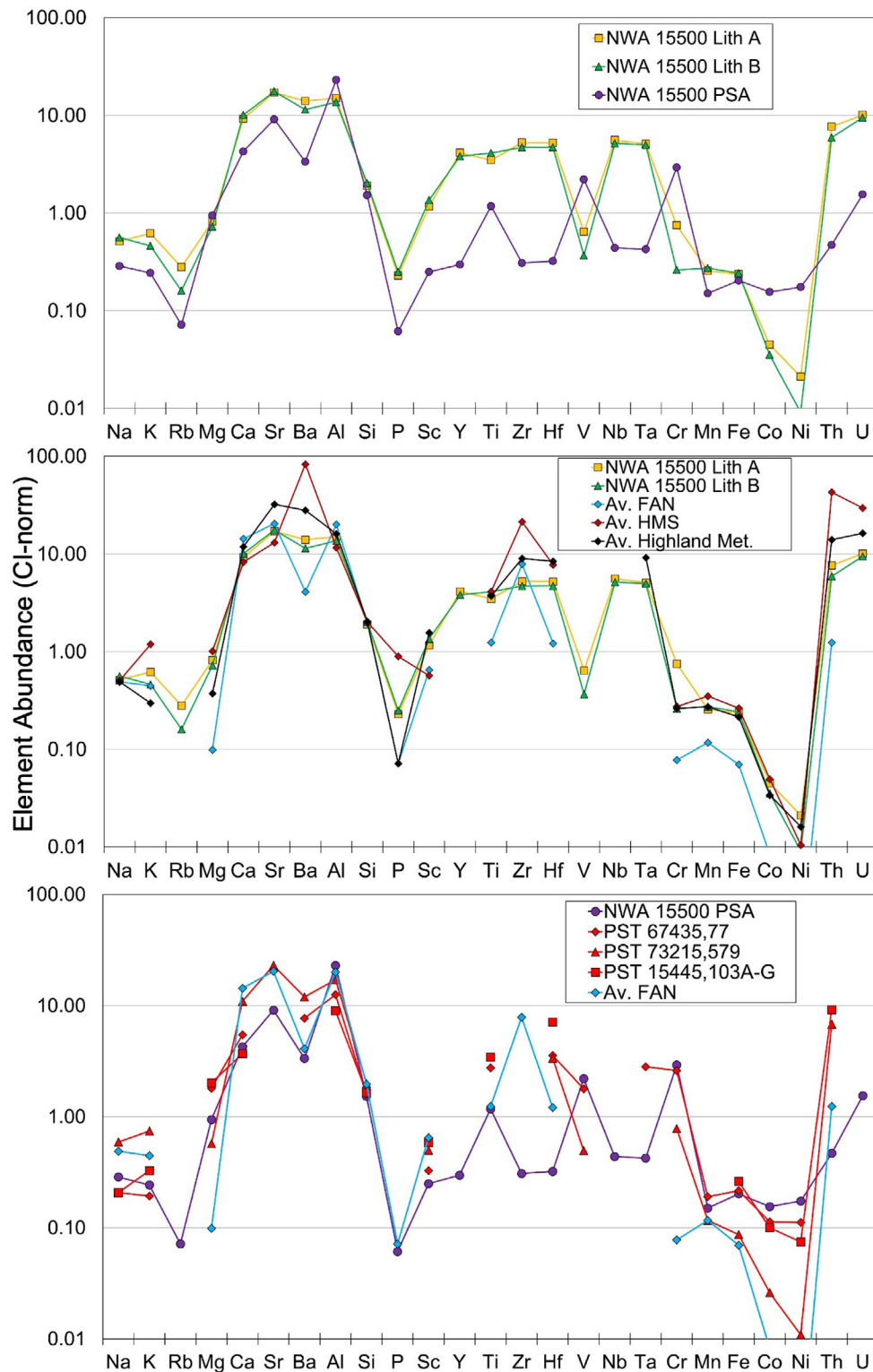
FIGURE 9. CI-normalized elemental spider diagram (CI-chondrite abundances from Anders and Grevesse, 1989) for (a) bulk compositions of NWA 15500 Lith A, Lith B, and a PSA clast separate (this work); (b) NWA 155500 Lith A and B and average Apollo FANs, High-Mg Suite (HMS) samples, and lunar highland meteorites (Cahill et al., 2004); and c) PSA clast separate (this work), average Apollo FANs, and individual PST samples 67435,77 (Ma et al., 1981), 73,215,579 (Neal and Taylor, 1998), and 15445,103A-G (Blanchard et al., 1976; Papike et al., 1998). (Color figure can be viewed at wileyonlinelibrary.com)
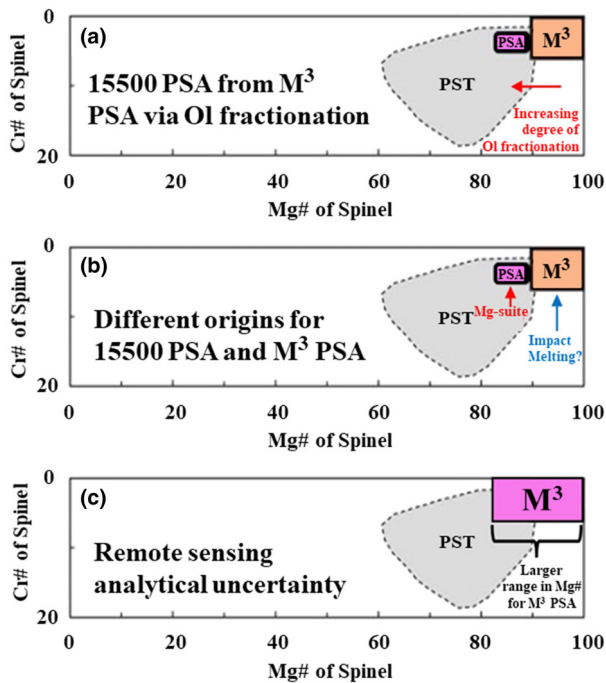
FIGURE 10. Various ideas for the compositional differences in spinel Mg# between NWA 15500 PSA and PSA estimated remotely by M^3 (Jackson et al., 2014). (Color figure can be viewed at wileyonlinelibrary.com)

from M^3 (Jackson et al., 2014), may indicate that the PSA clasts sampled in NWA 15500 are different from that of PSA observed by M^3. Observations of distinct Mg-spinel "flavors" within the Ingenii-Thomson region (Sodha & Dhingra, 2022) lend support to the existence of a compositional diversity in PSA spinel composition, which would fit with the idea that different exposures of PSA on the Moon were produced by varying degrees of assimilation by Mg-suite parent melts within a slightly variable Mg# range.

In scenario two (Figure 10b), PSA detected via remote sensing with Mg# >88 spinels (Jackson et al., 2014) may have formed by a different mechanism than NWA 15500 PSA. As an alternative model to magma–wallrock interactions at depth, it has been proposed that impact melting of troctolitic source rocks on the lunar surface and crystallization of spinel from the resulting high Mg# melt could plausibly create highly magnesian spinels (Treiman et al., 2019). This mechanism could be consistent with the presence of PSA outcrops within and along the walls of impact craters and basins (Pieters et al., 2014) and is supported by the presence of spinel-bearing (~0.2–5.2 vol% spinel) lithologies observed in lunar meteorite NWA 13191 (Xie et al., 2024) that chemically fit within the spinel compositional field of PSA estimated by M^3 and which display features that are consistent with impact melting of Mg-rich anorthosite precursors, such as small (<15 μm)

spinel grains, quench textures, and chemical zonation. However, it seems unlikely that the spinel-bearing clasts in NWA 13191 are actually the PSA lithology that is observed remotely, as spinel abundances from these clasts (<6 vol%) are much lower than that estimated for PSA (>20 vol%, Gross, Isaacson, et al., 2014), and it has been suggested that at least ~10 vol% spinel is required in order to generate noticeable reflectance spectra dominated by spinel (Gross et al., 2015).

In scenario three (Figure 10c), analytical uncertainty in the estimated M^3 PSA spinel compositional field due to space weathering effects and mixing with plagioclase, which would weaken the 1000 nm absorption band for PSA reflectance spectra independently of spinel Mg# (Jackson et al., 2014), may indicate that minor differences in spinel Mg# are negligible and that NWA 15500 PSA clasts do indeed sample remotely observed PSA. For example, the average spinel Mg# for NWA 15500 PSA C7 (87.7 ± 0.3 from EPMA data, Table 2) just barely makes the cutoff for the M^3 PSA spinel Mg# range (>88, Jackson et al., 2014); there may exist other PSA clasts from NWA 15500 or other rocks that record a higher spinel Mg# that overlaps with M^3 PSA.

Ultimately, without ground truth sampling of confirmed PSA exposures by future returned missions to the Moon, there is no way to differentiate between the three scenarios listed above. However, until then, based on the combination of spinel abundance and chemistry, NWA 15500 PSA constitutes the best "ground truth" candidate in our lunar sample collection of M^3 PSA.

Petrogenesis of NWA 15500 PSA, Lith A, and Lith B

As spinel is poikilitically enclosed in both plagioclase and olivine, and olivine primarily occurs along the margins of the PSA clasts (and is less abundant than plagioclase), this suggests a crystallization sequence for PSA that began spinel-saturated and ended with olivine crystallization (i.e., Liq → Liq + Sp → Liq + Sp + Pl → Liq + Sp + Pl + Ol) (Sheikh & Ruzicka, 2024). Because our calculated equilibration temperature (T_{eq}) range for the NWA 15500 PSA clasts (~1107–1189°C) is slightly lower than experimentally derived estimates of the Sp-Pl-Ol peritectic reaction temperature of the bulk system (~1225–1300°C, where previously crystallized spinel reacts with melt at this monoresorptional point to crystallize olivine + plagioclase; Prissel et al., 2016), this could indicate that either (1) there was not enough melt available to carry the peritectic reaction to completion (so T_{eq} represents a subsolidus re-equilibration temperature attained following solidification of PSA and minor cooling), or (2) T_{eq} represents an accurate lower bound estimate of the true peritectic reaction temperature of the system. In either scenario, following the crystallization of PSA at depth, impact

excavation (either by a large basin-forming impactor or by multiple smaller impactors) of PSA material to shallower depths (likely near to, or at the lunar surface) must have allowed rapid cooling to preserve the observed high-temperature Fe-Mg chemical equilibrium between olivine and spinel (Sheikh & Ruzicka, 2024); in contrast, slow cooling at depth would have resulted in substantial Ol-Sp Fe-Mg subsolidus re-equilibration as is evident in Mg-suite troctolites and dunites (Prissel et al., 2016) (Figure 6a). As a consequence of deformation induced by impact excavation, PSA material was brecciated into clasts, mineral grains were pervasively fractured, and exogenous metal + sulfide melts were likely mobilized into these fractures (forming metal grains with high Ni/Co, Day, 2020).

The nearly identical bulk chemical compositions of Lith A and Lith B and the texture of Lith B imply that Lith B formed directly by localized melting of Lith A during a relatively strong shock event. As Lith A is comprised primarily of anorthositic and olivine-bearing Mg-suite lithic clasts, this is consistent with the overall troctolitic mineralogy of Lith B. The slight enrichments in V, Cr, Co, and Ni in Lith A relative to Lith B that reflect the incorporation of PSA clasts/clast fragments suggest that less PSA was incorporated in Lith B. This could indicate either (1) a sampling bias or (2) reflect the tendency of PSA to not be incorporated into the melt that formed Lith B due to its relatively higher melting temperature compared to the other Lith A components.

The occurrence of both crystalline plagioclase and amorphous maskelynite ubiquitously in lithologies A and B, and within PSA clasts, provides support for the consolidation of NWA 15500 due to a late, strong shock (shock pressures <28 GPa, Fritz et al., 2019); this latest event may have been the same one that resulted in the ejection of the NWA 15500-producing meteoroid from the lunar surface.

CONCLUSIONS

We investigated the textural, mineralogical, and geochemical features of seven PSA clasts in lunar meteorite Northwest Africa (NWA) 15500. Our findings are consistent with the PSA clasts in NWA 15500 representing an Mg-suite lithology (with a genetic relationship to PST) formed by magma–wallrock interactions between anorthositic crust and plagioclase-undersaturated Mg-suite parental melts (Prissel et al., 2014). Following impact excavation of PSA material, NWA 15500 lithology A was assembled, and a later strong shock event resulted in localized melting to form lithology B. The lack of a noticeable incompatible element enrichment (i.e., KREEP component) in either the PSA clasts or in NWA 15500 indicates that NWA 15500 PSA is likely a farside lithology

of the Feldspathic Highlands Terrane (FHT) (Jolliff et al., 2000), supporting models for Mg-suite magmatism representing a global process not limited to the lunar nearside nor requiring contribution from a KREEP source (Prissel & Gross, 2020). Future age dating, spectral reflectance measurements, and geochemical modeling of PSA clasts in NWA 15500, and in recently classified lunar meteorite NWA 16400 (the most spinel-rich sample from the Moon, Sheikh et al., 2024) will be important for better understanding the complexities of lunar crust–mantle interactions and assimilation processes (Heinonen et al., 2021), the candidate Mg-suite parental melt compositions, the global extent of Mg-suite magmatism, and the link between PSA observed through remote sensing (Pieters et al., 2014) and "ground truth" PSA observed in lunar samples.

Data Availability Statement—The data that support the findings of this study are available in the supplementary material of this article.

Editorial Handling—Dr. Jeffrey Plescia and Dr. Kevin Righter

REFERENCES

Anders, E., and Grevesse, N. 1989. Abundances of the Elements: Meteoritic and Solar. *Geochimica et Cosmochimica Acta* 53: 197–214.

Bence, A. E., Taylor, S. R., Muir, P. M., Nance, W. B., Rudowski, R., and Ware, N. 1975. Chemical and Petrologic Relations among Lunar Highland Rock Types. *Abstracts of the Lunar and Planetary Science Conference* 6: 36–38.

Blanchard, D. P., Brannon, J. C., Haskin, L. A., and Jacobs, J. W. 1976. Sample 15445. Chemistry. In *Interdisciplinary Studies by the Imbrium Consortium*, edited by J. B. Adams, E. Anders, M. R. Dence, L. A. Haskin, J. W. Head, N. J. Hubbard, T. B. McCord, et al., vol. 2, 60. Cambridge, MA: Smithsonian Astrophysical Observatory.

Blanchard, D. P., Jacobs, J. W., and Brannon, J. C. 1977. Chemistry of ANT-Suite and Felsite Clasts from Consortium Breccia 73215 and of Gabbroic Anorthosite 79215. *8th Lunar Science Conference, Proceedings Volume 2*, 2507–24.

Cahill, J. T., Floss, C., Anand, M., Taylor, L. A., Nazarov, M. A., and Cohen, B. A. 2004. Petrogenesis of Lunar Highlands Meteorites: Dhofar 025, Dhofar 081, Dar al Gani 262, and Dar al Gani 400. *Meteoritics & Planetary Science* 39: 503–529.

Chen, H., Xie, L., Shu, Q., and Miao, B. 2023. Northwest Africa 12279: Evidence for the Interaction between Early Lunar Mantle Melt and Anorthositic Crust. *Journal of Geophysical Research: Planets* 128: E007844.

Day, J. M. D. 2020. Metal Grains in Lunar Rocks as Indicators of Igneous and Impact Processes. *Meteoritics & Planetary Science* 55: 1793–1807.

Elardo, S. M., Draper, D. S., and Shearer, C. K. 2011. Lunar Magma Ocean Crystallization Revisited: Bulk Composition, Early Cumulate Mineralogy, and the Source Regions of the Highlands Mg-Suite. *Geochimica et Cosmochimica Acta* 75: 3024–45.

Elardo, S. M., Pieters, C. M., Dhingra, D., Donaldson Hanna, K. L., Glotch, T. D., Greenhagen, B. T., Gross, J., et al. 2023. The Evolution of the Lunar Crust. In *New Views of the Moon 2, Reviews in Mineralogy and Geochemistry*, edited by C. R. Neil, L. R. Gaddis, B. L. Jolliff, S. J. Lawrence, S. J. Mackwell, C. K. Shearer, and S. N. Valencia, vol. 89, 293–338. Chantilly, VA: Mineralogical Society of America.

Elkins-Tanton, L. T., Burgess, S., and Yin, Q. Z. 2011. The Lunar Magma Ocean: Reconciling the Solidification Process with Lunar Petrology and Geochronology. *Earth and Planetary Science Letters* 304: 326–336.

Floss, C., James, O. B., McGee, J. J., and Crozaz, G. 1998. Lunar Ferroan Anorthosite Petrogenesis: Clues from Trace Element Distributions in FAN Subgroups. *Geochimica et Cosmochimica Acta* 62: 1255–83.

Fritz, J., Fernandes, V. A., Greshake, A., Holzwarth, A., and Böttger, U. 2019. On the Formation of Diaplectic Glass: Shock and Thermal Experiments with Plagioclase of Different Chemical Compositions. *Meteoritics & Planetary Science* 54: 1533–47.

Gattacceca, J., McCubbin, F. M., Grossman, J. N., Schrader, D. L., Chabot, N. L., D'Orazio, M., Goodrich, C., et al. 2023. The Meteoritical Bulletin, No. 111. *Meteoritics & Planetary Science* 58: 901–4. https://doi.org/10.1111/maps.13995.

Gross, J., Gillis-Davis, J., Isaacson, P. J., and Le, L. 2015. How Rich is Rich? Placing Constraints on the Abundance of Spinel in the Pink Spinel Anorthosite Lithology on the Moon Through Space Weathering. *46th Lunar and Planetary Science Conference*, abstract #2642.

Gross, J., Isaacson, P. J., Treiman, A. H., Le, L., and Gorman, J. K. 2014. Spinel-Rich Lithologies in the Lunar Crust: Linking Lunar Samples with Crystallization Experiments and Remote Sensing. *American Mineralogist* 99: 1849–59.

Gross, J., and Treiman, A. H. 2011. Unique Spinel-Rich Lithology in Lunar Meteorite ALHA 81005: Origin and Possible Connection to M3 Observations of the Farside Highlands. *Journal of Geophysical Research* 116: E10009.

Gross, J., Treiman, A. H., and Mercer, C. N. 2014. Lunar Feldspathic Meteorites: Constraints on the Geology of the Lunar Highlands, and the Origin of the Lunar Crust. *Earth and Planetary Science Letters* 388: 318–328.

Heinonen, J. S., Iles, K. A., Heinonen, A., Fred, R., Virtanen, V. J., Bohrson, W. A., and Spera, F. J. 2021. From Binary Mixing to Magma Chamber Simulator: Geochemical Modeling of Assimilation in Magmatic Systems. In *Crustal Magmatic System Evolution: Anatomy, Architecture, and Physico-Chemical Processes, Geophysical Monograph 264*, edited by M. Masotta, C. Beier, and S. Mollo, 151–176. Hoboken, NJ: Wiley.

Herzberg, C. T., and Baker, M. B. 1980. The Cordierite- to Spinel-Cataclasite Transition: Structure of the Lunar Crust. In *Proceedings of the Conference on the Lunar Highlands Crust*, edited by R. B. Merrill, and J. J. Papike, 113–132. New York and Oxford: Pergamon.

Jackson, C. R. M., Cheek, L. C., Williams, K. B., Donaldson, H. K., Pieters, C. M., Parman, S. W., Cooper, R. F., Dyar, M. D., Nelms, M., and Salvatore, M. R. 2014. Visible-Infrared Spectral Properties of Iron-Bearing Aluminate Spinel under Lunar-like Redox Conditions. *American Mineralogist* 99: 1821–33.

Jianping, L., Kornprobst, J., Vielzeuf, D., and Fabriès, J. 1995. An Improved Experimental Calibration of the Olivine-Spinel Geothermometer. *Chinese Journal of Geochemistry* 14: 68–77.

Jochum, K. P., Weis, U., Schwager, B., Stoll, B., Wilson, S. A., Haug, G. H., Andreae, M. O., and Enzweiler, J. 2015. Reference Values Following ISO Guidelines for Frequently Requested Rock Reference Materials. *Geostandards and Geoanalytical Research* 40: 333–350.

Jolliff, B. L., Gillis, J. J., Haskin, L. A., Korotev, R. L., and Wieczorek, M. A. 2000. Major Lunar Crustal Terranes: Surface Expressions and Crust-Mantle Origins. *Journal of Geophysical Research* 105: 4197–4216.

Karner, J., Papike, J. J., and Shearer, C. K. 2006. Comparative Planetary Mineralogy: Pyroxene Major- and Minor-Element Chemistry and Partitioning of Vanadium between Pyroxene and Melt in Planetary Basalts. *American Mineralogist* 91: 1574–82.

Korotev, R. L. 2005. Lunar Geochemistry as Told by Lunar Meteorites. *Chemie der Erde* 65: 297–346.

Korotev, R. L., and Irving, A. J. 2021. Lunar Meteorites from Northern Africa. *Meteoritics & Planetary Science* 56: 206–240.

Ma, M.-S., Schmitt, R. A., Taylor, G. J., Warner, R. D., and Keil, K. 1981. Chemical and Petrographic Study of Spinel Troctolite in 67435: Implications for the Origin of Mg-Rich Plutonic Rocks. *12th Lunar and Planetary Science Conference*, pp. 640–642.

Neal, C. R., and Taylor, L. A. 1998. Exploring the Complexities of the Serenitatis Basin: Breccia Clasts from Apollo 17. *International Geology Review* 40: 945–962.

Papike, J. J., Karner, J. M., and Shearer, C. K. 2003. Determination of Planetary Basalt Parentage: A Simple Technique Using the Electron Microprobe. *American Mineralogist* 88: 469–472.

Papike, J. J., Ryder, G., and Shearer, C. K. 1998. Chapter 5. Lunar samples. In *Planetary Materials, Reviews in Mineralogy and Geochemistry*, edited by J. J. Papike, vol. 36, 1–234. Washington, DC: Mineralogical Society of America.

Pieters, C. M., Besse, S., Boardman, J., Buratti, B., Cheek, L., Clark, R. N., Combe, J. P., et al. 2011. Mg-Spinel Lithology: A New Rock Type on the Lunar Farside. *Journal of Geophysical Research: Planets* 116: E00G08.

Pieters, C. M., Donaldson, H. K., Cheek, L., Dhingra, D., Prissel, T., Jackson, C., Moriarty, D., Parman, S., and Taylor, L. A. 2014. The Distribution of Mg-Spinel across the Moon and Constraints on Crustal Origin. *American Mineralogist* 99: 1893–1910.

Prissel, T. C., and Gross, J. 2020. On the Petrogenesis of Lunar Troctolites: New Insights into Cumulate Mantle Overturn & Mantle Exposures in Impact Basins. *Earth and Planetary Science Letters* 551: 116531.

Prissel, T. C., Parman, S. W., and Head, J. W. 2016. Formation of the Lunar Highlands Mg-Suite as Told by Spinel. *American Mineralogist* 101: 1624–35.

Prissel, T. C., Parman, S. W., Jackson, C. R. M., Rutherford, M. J., Hess, P. C., Head, J. W., Cheek, L., Dhingra, D., and Pieters, C. M. 2014. Pink Moon: The Petrogenesis of Pink Spinel Anorthosites and Implications Concerning Mg-Suite Magmatism. *Earth and Planetary Science Letters* 403: 144–156.

Ryder, G. 1991. Lunar Ferroan Anorthosites and Mare Basalt Sources: The Mixed Connection. *Geophysical Research Letters* 18: 2065–68.

Schmidt, M. W., and Kraettli, G. 2022. Experimental Crystallization of the Lunar Magma Ocean, Initial Selenotherm and Density Stratification, and Implications for Crust Formation, Overturn and the Bulk Silicate Moon Composition. *Journal of Geophysical Research: Planets* 127: 1–32.

Shearer, C. K., Elardo, S. M., Petro, N. E., Borg, L. E., and McCubbin, F. M. 2015. Origin of the Lunar Highlands Mg-Suite: An Integrated Petrology, Geochemistry, Chronology, and Remote Sensing Perspective. *American Mineralogist* 100: 294–325.

Shearer, C. K., and Papike, J. J. 1999. Magmatic Evolution of the Moon. *American Mineralogist* 84: 1469–94.

Sheikh, D., Ruzicka, A., Hutson, M., and Zlimen, C. 2023. Pink Spinel Anorthosite (PSA) Clasts in Lunar Dimict Breccia Northwest Africa (NWA) 15500: Evidence for a Petrogenetic Link between PSA and Mg-Suite *54th Lunar and Planetary Science Conference*, abstract #2066.

Sheikh, D., and Ruzicka, A. M. 2024. Application of Electron Backscatter Diffraction (EBSD) to Investigate the Petrogenesis and Shock Deformation History of a Pink Spinel Anorthosite (PSA) Clast in Lunar Meteorite Northwest Africa (NWA) 15500. 86th Annual Meeting of the Meteoritical Society, abstract #6468.

Sheikh, D., Ruzicka, A. M., and Hutson, M. L. 2024. The Most Spinel-Rich Sample from the Moon: A First Look at Pink Spinel Anorthosite (PSA), Pink Spinel Pyroxenite (PSP), and Spinel-Cordierite Assemblages (SCA) in Northwest Africa (NWA) 16400. *55th Lunar and Planetary Science Conference*, abstract #2023.

Sheikh, D., Ruzicka, A. M., Hutson, M. L., and Stream, M. 2022. Dunite Clast in Lunar Meteorite Northwest Africa (NWA) 14900: Mantle Derived? 84th Annual Meeting of the Meteoritical Society, abstract #6077.

Sodha, G., and Dhingra, D. 2022. Mg-Spinel Exposures in the South-Pole Aitken (SPA) Basin: New Insights into the Stratigraphic Relationships, Spatial Distribution and Spectral Varieties. *53rd Lunar and Planetary Science Conference*, abstract #2894.

Treiman, A. H., Kulis, M. J., and Glazner, A. F. 2019. Spinel-Anorthosites on the Moon: Impact Melt Origins Suggested by Enthalpy Constraint. *American Mineralogist* 104: 370–384.

Warren, P. H. 2012. Let's Get Real: Not Every Lunar Rock Sample Is Big Enough to be Representative for Every Purpose Second Conference on the Lunar Highlands Crust, abstract #9034.

Warren, P. H., and Taylor, G. J. 2014. The Moon. In *Treatise on Geochemistry*, edited by H. D. Holland, and K. K. Turekian, 2nd ed., vol. 2, 213–250. Houston, TX: Elsevier.

Warren, P. H., and Wasson, J. T. 1980. Further Foraging for Pristine Nonmare Rocks: Correlations between Geochemistry and Longitude. *11th Lunar and Planetary Science Conference*, pp. 431–470.

Williams, K. B., Jackson, C. R. M., Cheek, L. C., Donaldson-Hanna, K. L., Parman, S. W., Pieters, C. M., Dyar, M. D., and Prissel, T. C. 2016. Reflectance Spectroscopy of Chromium-Bearing Spinel with Application to Recent Orbital Data from the Moon. *American Mineralogist* 101: 726–734.

Xie, L. F., Chen, H. Y., Miao, B. K., Song, W. L., Xia, Z. P., Zhang, C. T., Chen, G. Z., Zhang, J. Y., Zhao, S. Z., and Gao, X. K. 2024. A Possible Origin of the Lunar Spinel-Bearing Lithologies as Told by the Meteorite NWA 13191. *American Mineralogist* 109: 457–470.

SUPPORTING INFORMATION

Additional supporting information may be found in the online version of this article.

Table S1. Thermometry curve calculations.
Table S2. Bulk ICP-MS chemical data.
Figure S1. Images of hand specimens.
Figure S2. Images of thin sections.
Figure S3. BSE and EDS map images for CML 1625-2.
Data S1. EPMA data and analysis locations.
Data S2. SEM-EDS data for lithology A and analysis locations.
Data S3. SEM-EDS data for lithology A-B contact area and analysis locations.
Data S4. SEM-EDS data for lithology B and analysis locations.
Data S5. SEM-EDS data for PSA clast C1 and analysis locations.
Data S6. SEM-EDS data for PSA clast C2 and analysis locations.

Data S7. SEM-EDS data for PSA clast C3 and analysis locations.

Data S8. SEM-EDS data for PSA clast C4 and analysis locations.

Data S9. SEM-EDS data for PSA clast C5 and analysis locations.

Data S10. SEM-EDS data for PSA clast C6 and analysis locations.

Data S11. SEM-EDS data for PSA clast C7 and analysis locations.